PCCP

Accepted Manuscript

ROYAL SOCIETY OF CHEMISTRY

www.rsc.org/pccp

Cite this: DOI: 10.1039/c0xx00000x

www.rsc.org/xxxxxx

ARTICLE TYPE

A blue-emitting Sc silicate phosphor for ultraviolet excited light-emitting diodes

Qian Wang,[a] Ge Zhu,[a] Shuangyu Xin,[a] Xin Ding,[a] Ju Xu,[b] Yuansheng Wang,[b] Yuhua Wang[a]*

Received (in XXX, XXX) Xth XXXXXXXXX 20XX, Accepted Xth XXXXXXXXX 20XX
DOI: 10.1039/b000000x

A blue-emitting phosphor $BaSc_2Si_3O_{10}$: Eu^{2+} was synthesized by the conventional solid state reaction. The crystallographic occupancy of Eu^{2+} in the $BaSc_2Si_3O_{10}$ matrix was studied based on the Rietveld refinements results and the photoluminescence properties. $BaSc_2Si_3O_{10}$ exhibit blue emission ascribed to $^3T_2$-$^1A_1$ and $^3T_1$-$^1A_1$ charge transfer of SiO_4^{4-} excited by 360 nm. All the phosphors of $BaSc_2Si_3O_{10}$: Eu^{2+} exhibit strong broad absorption bands in the near ultraviolet range, and give abnormal blue emission upon 330 nm excitation. The abnormal phenomenon was explored in detail through many experimental evidences. The concentration of Eu^{2+} is optimized to be 3 mol% according to emission intensity and the quenching mechanism is verified to be the quadrupole-quadrupole interaction. The CIE coordinates of $BaSc_2Si_3O_{10}$: $0.03Eu^{2+}$ are calculated to be (0.15, 0.05) and $BaSc_2Si_3O_{10}$: $0.03Eu^{2+}$ shows similar thermal stability to commercial $BaMgAl_{10}O_{17}$:Eu^{2+}.

1. Introduction

Recently, phosphor conversion white light-emitting diodes (w-LEDs) have been attracted much attention owing to the merits of long operation time, high energy efficiency, low thermal radiation.[1,2] At present, the combination of the ultraviolet (UV)/near-UV (n-UV) LED chips with tri-color phosphors (red/green/blue) are employed to realize the practical white light emission.[3,4] The present commercial blue phosphor $BaMgAl_{10}O_{17}$: Eu^{2+} and $(Sr, Ba, Ca)_3MgSi_2O_8$: Eu^{2+} have high efficiency but poor thermal stability.[5,6] Hence, the research on new blue phosphors with excellent thermal stability for n-UV pumped LEDs is necessary.

Eu^{2+} and Ce^{3+} are the most commonly used activator for blue emitting phosphors.[7, 8] The emission of Eu^{2+} originating from the $4f^65d - 4f^7$ electronic transition is sensitive to the crystal field and covalency, exhibits broad emission bands from blue to red.[9,10] Eu^{2+}-doped phosphors usually reveal strong absorption band in the region of 250-400 nm, which matches well with the emission of UV and n-UV LED chips. Meanwhile, the small Stokes shift and short decay time of Eu^{2+} have attracted a lot of interesting, such as $Ba_2Ca(PO_4)_2$: Eu^{2+},[11] $Ca_4(PO_4)_2O$: Eu^{2+},[12] $CaAl_2Si_2O_8$: Eu^{2+}[13] and $Na_3(Y, Sc)Si_3O_9$: Eu^{2+}.[14]

Among a lot of possible matrices, silicates compounds are considered to be good candidates as the host structure due to several virtues of excellent chemical and thermal stability, resistance to moisture and their abundance in nature.[15] In silicates matrices, Sc silicates display the excellent photoluminescence properties on account of the stable physical and chemical properties and the rich crystal chemistry environment for the doped rare earth ions,[16] such as $Ca_3Sc_2Si_3O_{12}$: Ce^{3+},[17] $NaBaScSi_2O_7$: Eu^{2+}.[18] This proves Sc silicates can serve as the suitable phosphor hosts for LED application. A family of trisilicates $BaRe_2Si_3O_{10}$ (Re = Gd, Er, Yb, Sc) was firstly reported by M. Wierzbicka-Wieczorek et al. in 2010.[19] Their topology is characterised by horseshoe-shaped trisilicate (Si_3O_{10}) groups and zigzag chains of edge-sharing distorted ReO_6 octahedra (Re = Gd, Er, Yb, Sc). In this paper, the structure and luminescence properties of $BaSc_2Si_3O_{10}$: Eu^{2+} are explored. There are two coordination environments of cations: Ba^{2+} and Sc^{3+} in $BaSc_2Si_3O_{10}$. In our work, the radius percentage difference between the Eu^{2+} and Ba^{2+}, Sc^{3+} are calculated to be 11.9 % and 57 %, respectively. However, the radius percentage difference less than 30% is the necessary factor for the formation of solid solution. Moreover, the rare earth take place the sites of Na, Ca and Na, not Sc, in $Na_3(Y,Sc)Si_3O_9$: Eu^{2+},[14] $Ca_3Sc_2Si_3O_{12}$: Ce^{3+},[17] and $NaBaScSi_2O_7$: Eu^{2+},[18] respectively. Thus, there is only one suitable cationic site (Ba^{2+}) for Eu^{2+} in $BaSc_2Si_3O_{10}$, then a symmetry emission should be expected.[20] However, the emission of $BaSc_2Si_3O_{10}$: Eu^{2+} is composed by two emission band. We think it is an abnormal phenomenon and carefully analyse crystallographic occupancy of Eu^{2+} by the Rietveld analysis and the photoluminescence properties. In this study, based on the basic research and application for LEDs, we measured the luminescence efficiency, thermal quenching property and color chromaticity of the new blue phosphor $BaSc_2Si_3O_{10}$: Eu^{2+}.

2. Experimental

The polycrystalline samples with nominal chemical formula $Ba_{1-x}Eu_xSc_2Si_3O_{10}$ (x = 0.005-0.11) were prepared by the conventional solid-state reaction in one step. $BaCO_3$ (99.9%), Sc_2O_3 (99.9%), H_2SiO_3 (99.8%) and Eu_2O_3 (99.99%) were used as raw materials.

The raw materials were weighed out according to the stoichiometric ratio of the desired compositions and thoroughly mixed by grinding evenly in an agate mortar. Afterward, the obtained product was annealed at 1350 °C for 8 h under a reducing 5% H_2/95% N_2 atmosphere. Finally, the sample cooled down to room temperature and some white polycrystalline powder was obtained.

The crystalline phases of samples were recorded by using a Rigaku D/Max-2400 X-ray diffractometer (XRD) with Ni-filtered Cu Ka radiation, operating at 40 kV, 60 mA. The photoluminescence excitation (PLE) and emission (PL) spectra, quantum efficiency and decay curves of the samples were measured using an FLS-920T fluorescence spectrophotometer equipped with a 450 W Xe light source. The emission spectra and decay curves at low temperature (from 77 K to 298 K) were measured by using FLS-920T fluorescence spectrophotometer under the protection of liquid nitrogen. The morphologies of samples were observed by transmission electron microscopy (TEM) and high-resolution transmission electron microscopy (HRTEM), the selected area electron diffraction (SAED), and the energy-dispersive X-ray diffraction (EDX) was obtained by FEI Tecnai F30, operating at 300 kV. The temperature-dependent photoluminescent property was tested using a heating apparatus (TAP-02) in combination with PL equipment.

3. Results and discussion

3.1 Phase identification and crystal structure

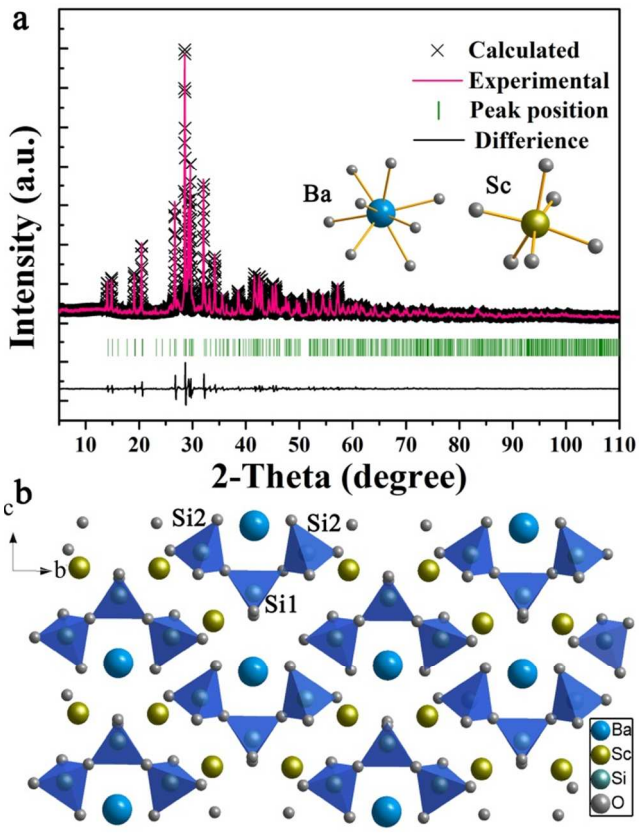

Fig.1 (a) XRD refinement results of $BaSc_2Si_3O_{10}$: $0.01Eu^{2+}$ using the MS program. (b) Structure view of $BaSc_2Si_3O_{10}$ along [100]

The powder XRD of our prepared samples was performed to detect the phase purity. Figure 1(a) shows Rietveld structural refinements of the powder diffraction patterns of $BaSc_2Si_3O_{10}$: $0.01Eu^{2+}$. The black crosses and pink solid lines are calculated patterns and experimental patterns, respectively. The green short vertical lines show the position of the Bragg reflections of the calculated pattern. The difference between the experimental and calculated patterns is plotted by the black line at the bottom. The refined unit cell parameters and residual factors are summarized in Table 1. $BaSc_2Si_3O_{10}$ has a monoclinic structure with space group $P2_1/m$,[19] as shown in Fig. 1(b). The asymmetric unit of $BaSc_2Si_3O_{10}$ contains one Ba, one Sc, two Si and six O atoms. The structure of $BaSc_2Si_3O_{10}$ composed of three SiO_4 tetrahedra, forms a horseshoe-shaped trisilicate Si_3O_{10} group, ScO_6 octahedra and BaO_8 polyhedron. The Ba, Si1, O1 and O2 atoms are located on mirror planes (y = 1/4), while all remaining atoms are in general positions. It is noteworthy that the Si_3O_{10} group, composed of a central $Si1O_4$ tetrahedron corner-linked to two symmetry–equivalent terminal $Si2O_4$ tetrahedra, is located on mirror planes parallel to (010) at y= 1/4 and 3/4. In $BaSc_2Si_3O_{10}$, Ba^{2+} are located in voids consisted of ScO_6 octahedron and SiO_4 tetrahedron. The structure of $BaSc_2Si_3O_{10}$ offers two types of cation sites for occupancy by guest cations: type I with divalent Ba sites having 8-fold coordination and type II with trivalent Sc^{3+} sites in ScO_6 polyhedra. The effective ionic radii of Ba^{2+} and Sc^{3+} are 1.42 and 0.745 Å, and the ionic radii for eight- and six-coordinated Eu^{2+} are 1.25 and 1.17 Å.[21] Therefore, based on the comparison of the effective ionic radii of cations, Eu^{2+} is likely to enter into the Ba^{2+} sites in this series of samples. Furthermore, an acceptable percentage difference in ion radii between doped and substituted ions must not exceed 30 %. The radius percentage difference between the doped Eu^{2+} and the possible substituted ions (Ba^{2+}, Sc^{3+}) can be calculated based on the following equation:[22]

$$D_r = 100 \times [R_m(CN) - R_d(CN)]/R_m(CN)$$

where D_r is the radius percentage difference; CN is the coordination number; $R_m(CN)$ is the radius of the host cation; and $R_d(CN)$ is the radius of the doped ion. The values of D_r for Eu^{2+} in Ba^{2+} and Sc^{3+} are determined to be 11.9 % and 57 %, respectively. Hence, it is reasonable that Eu^{2+} enters into the Ba^{2+} sites.

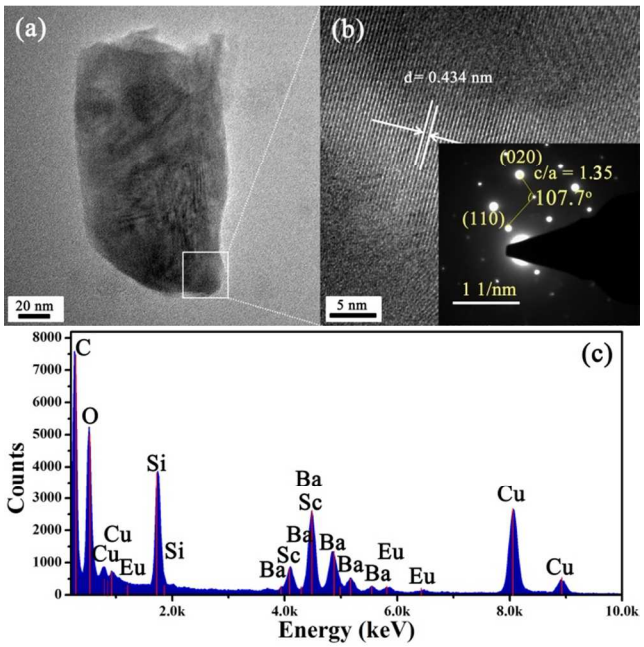

Fig.2 (a) TEM image of $BaSc_2Si_3O_{10}$: Eu^{2+} (b) the corresponding HRTEM image and the SAED pattern (c) EDX analysis.

Figure 2(a) shows a typical TEM image of a single $BaSc_2Si_3O_{10}$: Eu^{2+} particle. The corresponding high-magnification TEM image at the edge of the $BaSc_2Si_3O_{10}$: Eu^{2+} particle, as shown in Fig. 2(b), clearly displays the lattice fringes. The lattice spacing is 0.434 nm, corresponding to the (021) planes of $BaSc_2Si_3O_{10}$: Eu^{2+}. The inset of Fig. 2(b) shows the SAED patterns confirming the single phase of $BaSc_2Si_3O_{10}$: Eu^{2+} is formed. In the SAED patterns, c/a can be measured as about 1.35 and the angle between them is 107.7°. According to the crystallographic data, theoretical c/a in $BaSc_2Si_3O_{10}$ is 1.25 and the angle is 107.06°. The EDX analysis spectrum of $BaSc_2Si_3O_{10}$: Eu^{2+} is given in Fig. 2(c). All the composing elements of the sample have been detected, and no other impure elements are found.

Table 1 Crystallographic Data and Reliability Factor of $BaSc_2Si_3O_{12}$: xEu^{2+} (x = 0–0.05) Samples

sample	x = 0	x = 0.005	x = 0.01	x = 0.05
a (Å)	5.27162	5.27516	5.2817	5.27851
b (Å)	11.91488	11.92276	11.9374	11.93607
c (Å)	6.58826	6.59290	6.6061	6.60343
V (Å^3)	395.61	396.45	398.19	397.88
R_p	9.56 %	9.56 %	8.45 %	9.87 %
R_{wp}	12.91 %	12.55 %	11.07 %	13.20 %

3.2 Photoluminescence properties of $BaSc_2Si_3O_{10}$ and $BaSc_2Si_3O_{10}$: Eu^{2+}

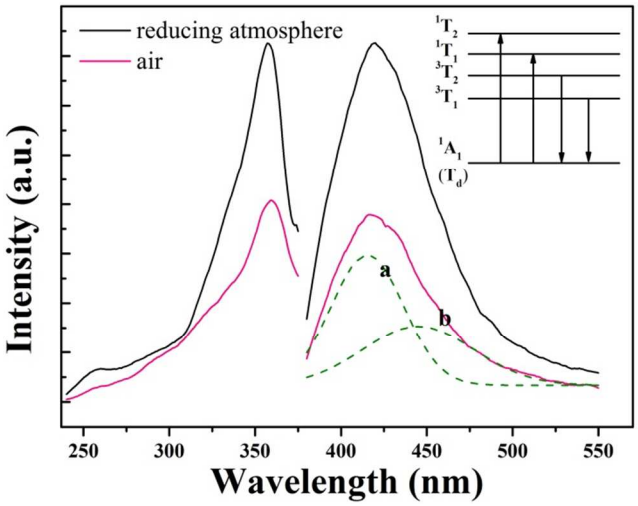

Fig. 3 The PLE (λ_{em} = 421 nm) and PL (λ_{ex} = 360 nm) spectra of $BaSc_2Si_3O_{10}$ obtained in air (red lines) and reducing atmosphere (black lines).

The PLE and PL spectra of $BaSc_2Si_3O_{10}$ are shown in Fig. 3. The red and black lines denote the excitation and emission spectra of $BaSc_2Si_3O_{10}$ in air and reducing atmosphere, respectively. The excitation band monitored by 426 nm is made up of a strong band centered at 360 nm and a weak one peaked at 257 nm. The two excitation bands centered at 360 nm and 257 nm can be associated with the $^1A_1$-$^1T_1$ and $^1A_1$-$^1T_2$ charge transfer of SiO_4^{4-}, respectively.[22] Under the excitation of 360 nm, the emission spectrum exhibits a broad change transfer band range from 380 to 550 nm located at 420 nm, as shown in Fig. 3. The broad emission band can be fitted into two Gaussian components, presented as the dotted line in Fig. 3. The higher-energy component (line a) centered at 415 nm and the lower-energy component (line b) centered at 445 nm are attributed to the $^3T_2$-$^1A_1$ and $^3T_1$-$^1A_1$ charge transfer of SiO_4^{4-}, respectively.[23] The photoluminescence properties of the $BaSc_2Si_3O_{10}$ samples calcined in a reducing atmosphere and that of air-calcined samples are compared to show that the calcined atmosphere also affects the photoluminescence properties of phosphors. Both the spectra are similar except for the peak intensity. The photoluminescence intensity is enhanced by 191 % while calcined in a reducing atmosphere compared with the air-calcined phosphor. In fact, the calcining in air atmosphere induces the diffusion of oxygen ions into the $BaSc_2Si_3O_{10}$ particle thus lowering the oxygen vacancy concentration. Calcining in a reducing atmosphere induces the oxygen diffusion out of the sample, increases of oxygen vacancy.[24] Here, the oxygen vacancy deficiency is considered to be responsible for the enhancement of photoluminescence intensity.

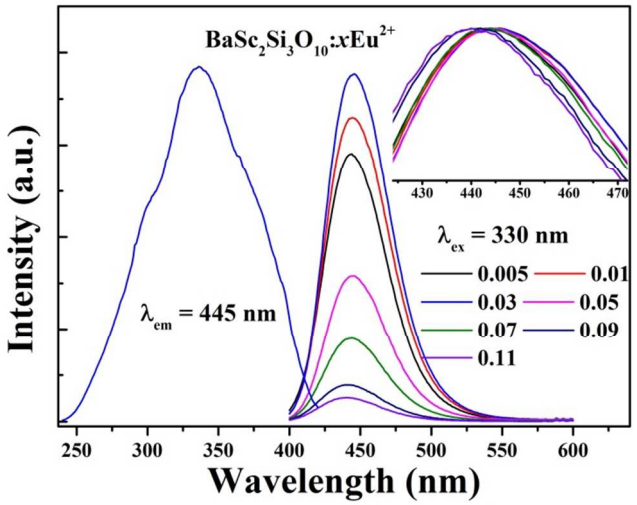

Fig.4 PLE (λ_{em} = 445 nm) and PL (λ_{ex} = 330 nm) spectra for $BaSc_2Si_3O_{10}$: xEu^{2+} ($0.005 \le x \le 0.11$) phosphors. The inset shows the normalized emission spectra.

The PLE spectrum of the selected $BaSc_2Si_3O_{10}$: $0.03Eu^{2+}$ and variations PL spectra of $BaSc_2Si_3O_{10}$: xEu^{2+} ($0.005 \le x \le 0.11$) are revealed in Fig. 4. The PLE spectrum of the phosphor monitored by 445 nm shows characteristic excitation broad band of Eu^{2+} in the range from 250 to 420 nm according with the emission light from UV-LED chips. Besides, the PLE spectrum contains three distinct bands originating from the $4f^7$ ground state to different excited states of Eu^{2+}. Upon the excitation of 330 nm, the PL spectra show broad band extending from 420 to 520 nm centered at 445 nm attributed to the transition from lower $4f^65d^1$ excited states to the quasi-degenerate $^8S_{7/2}$ ground state of Eu^{2+}.[25] The lowest energy zero phonon line of $BaSc_2Si_3O_{10}$: Eu^{2+} is estimated at about 409 nm, which is empirically determined as the intersection point of the excitation and emission spectra. The degree of the non-radiative relaxation of rare earth ions and the rigid of host lattice can be measured by the value of Stokes shift. The Stokes shift of $BaSc_2Si_3O_{10}$: Eu^{2+} is calculated to be 0.491 eV, which can be roughly estimated as twice of the energy difference between the peak energy of the emission band and lowest energy zero phonon line.[26] The Eu^{2+} content dependent PL intensities are drawn in Fig. 4. Obviously, the optimum Eu^{2+} concentration is 0.03 and then the PL intensities decrease with increasing Eu^{2+} concentration due to the concentration quenching effect. The CIE coordinates of $BaSc_2Si_3O_{10}$: $0.03Eu^{2+}$ are calculated to be (0.15, 0.05) indicating good blue emitting light. According to the Dexter's theory, concentration quenching is mainly caused by the non-radiative energy migration among the activators due to the exchange interaction or multipole–multipole interaction.[27] It is well-known that the interaction type between activators can be calculated by the following equation:[28]

$$\frac{I}{x} = K\left[1 + \beta(x)^{\frac{\theta}{3}}\right]^{-1}$$

Where x is the activator concentration, which is higher than the critical concentration; I/x is the emission intensity (I) per activator concentration (x); K and β are constants for the same excitation condition for a given host crystal; and θ is a function of multipole–multipole interaction. It was reported that three values of θ stands for the energy transfer among the nearest neighbor ions as θ = 6, 8, and 10 represent the dipole–dipole, dipole–quadrupole, and quadrupole–quadrupole interactions, respectively. The inset of Fig. 5 plots the dependence of log (I/x) on log (x) and with a slop of (-θ/3) is obtained to be -3.37. Then the value of θ can be determined to be 10.11 which is close to 10, meaning that the quenching is quadrupole–quadrupole interactions in present $BaSc_2Si_3O_{10}$: xEu^{2+} phosphors.

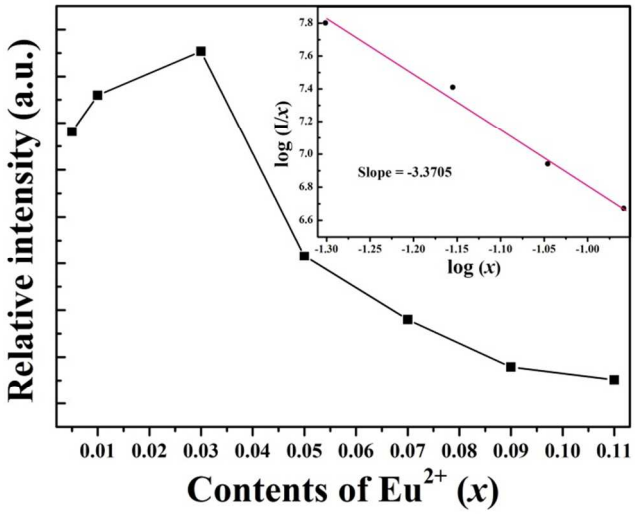

Fig. 5 PL intensities of $BaSc_2Si_3O_{10}$: xEu^{2+} as afunction of Eu^{2+} content. The inset shows the relationships of log (x) versus log (I/x).

3.3 The analysis of the abnormal phenomenon

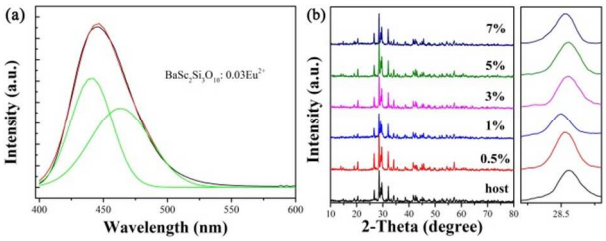

Fig.6 (a) Gaussian curves of $BaSc_2Si_3O_{10}$: $0.03Eu^{2+}$ and (b) XRD patterns of $BaSc_2Si_3O_{10}$: xEu^{2+} (x = 0, 0.005, 0.01, 0.03, 0.05 and 0.07) phosphors.

Interesting, $BaSc_2Si_3O_{10}$: Eu^{2+} shows a broad and abnormal asymmetry emission band with a tail on the long-wavelength side. The broad band can be fitted into two bands peaking at 440 and 464 nm by Gaussian curves as shown in Fig. 6(a). It should be noted that there is only one Ba site in $BaSc_2Si_3O_{10}$, and a symmetry emission should be expected. In Fig.4, except for the emission intensity, the PL spectra have subtle special changes in the spectra configuration. As the Eu^{2+} concentration increasing, the emission spectrum shifts to longer wavelength (red shift) and then to shorter wavelength (blue shift). There are three possible reasons are proposed as follows to explain the red shift. First, the energy transfer from Eu^{2+} ions at higher levels of 5d to those at lower levels of 5d was promoted with an increase of Eu^{2+} concentration, which results in red shifts in the emission spectrum. In addition, the reabsorption begin to reduce the high-energy wing of Eu^{2+} emission band with increasing Eu^{2+} concentration, which also cause the red shift of the emission band. Furthermore, the Eu^{2+} ionic radius is smaller than Ba^{2+}, then the crystal field may become stronger, which results in a larger split of 5d levels

and exhibits a red shift in the spectra. However, these reasons could not explain the further blue shift. Accordingly, the partial Eu^{2+} enter into Sc^{3+} site is speculated to be the possible reason for this abnormal asymmetry emission band. Fig. 6(b) depicts the XRD patterns of $BaSc_2Si_3O_{10}$ and Eu^{2+} activated $BaSc_2Si_3O_{10}$ with different Eu^{2+} contents. Compared with the XRD pattern of host, when the Eu^{2+} content is low, the diffraction peaks are shifted a little to lower angles implies Eu^{2+} replace smaller ions according to the Bragg equation. Then the diffraction peaks of samples are shifted to higher angles as the increase of Eu^{2+} concentration, originating from Eu^{2+} replacing bigger ions. In $BaSc_2Si_3O_{10}$, the ionic radius of Sc^{3+} is smaller than Eu^{2+} and Ba^{2+} is bigger than Eu^{2+}. Moreover, it is obvious that the unit cell parameters increased firstly and then slightly reduced with the increase of Eu^{2+}, shown in Table 1. These results indicate Eu^{2+} likely occupy Sc^{3+} site at low concentration of Eu^{2+}, and then occupy Ba^{2+} site with the increase of Eu^{2+} content.

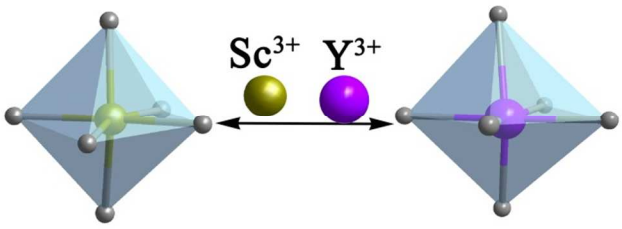

Fig. 7. Schematic diagrams of Sc^{3+} in $BaScSi_3O_{10}$ and Y^{3+} in $BaY_2Si_3O_{10}$.

In the structure of $BaReSi_3O_{10}$, the space size of Re is tunable because it can replaced by different trivalent ions, such as Gd^{3+}, Yb^{3+}, Er^{3+}[19] and Y^{3+},[29] which show bigger size than Sc^{3+}. The radius and values of D_r between Eu^{2+} and these rare earth ions are shown in Table 2. Figure 7 shows the Schematic diagram for the tunable space size of Re in $BaReSi_3O_{10}$ (Re = Sc, Y). Therefore, even though the value of D_r is much higher than 30% when Eu^{2+} enters Sc^{3+} site, there are still enough space for Eu^{2+} in $BaSc_2Si_3O_{10}$. Therefore, it is possible for Eu^{2+} to enter into Sc^{3+} site.

Table 2 The radius and values of D_r between Eu^{2+} and these rare earth ions

Rare earth	Sc^{3+}	Gd^{3+}	Yb^{3+}	Er^{3+}	Y^{3+}	Eu^{2+}
Radius (Å)	0.745	0.93	0.868	0.89	0.90	1.17
D_r (%)	57	25	34	31	30	

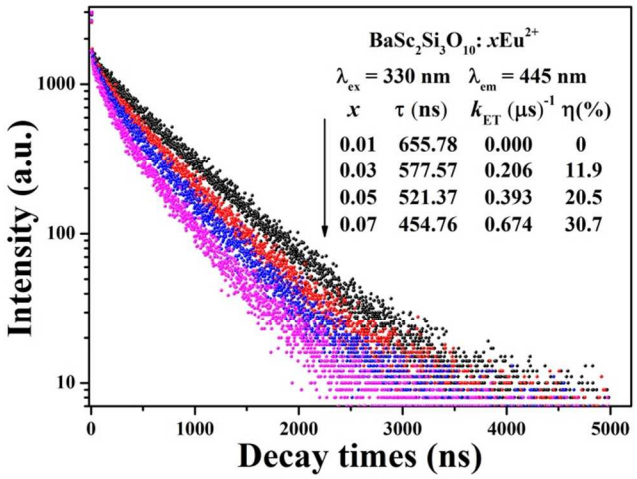

Fig. 8 Decay curves of $BaSc_2Si_3O_{10}$: xEu^{2+} phosphors with different Eu^{2+} contents.

The decay curves of $BaSc_2Si_3O_{10}$: xEu^{2+} were performed and shown in Fig. 8. All the decay curves could be well fitted with not a single exponential but second-order exponential decay mode, demonstrating that there are two light luminescent centers in the phosphor. The average decay times (τ) can be determined by the formula given in the following:[30]

$$\tau = \left(A_1{\tau_1}^2 + A_2{\tau_2}^2\right)/(A_1\tau_1 + A_2\tau_2)$$

where A_1 and A_2 are constants, and τ_1 and τ_2 are rapid and slow lifetimes for the exponential components, respectively. As can be seen from Fig. 8, the values of decay time decrease from 655.78 to 454.76 ns when the doped Eu^{2+} concentration increased from 0.01 to 0.07 mol%, which is a typical sign of energy transfer and eventually causes concentration quenching. The values of energy transfer rate ($k_{ET} = 1/\tau - 1/\tau_0$) and efficiency ($\eta = 100(1 - \tau/\tau_0)$) have been calculated and shown in Fig. 8. The maximum energy transfer rate (k_{ET}) and efficiency (η) are calculated to be 0.674 μs^{-1} and 30.7%, respectively.

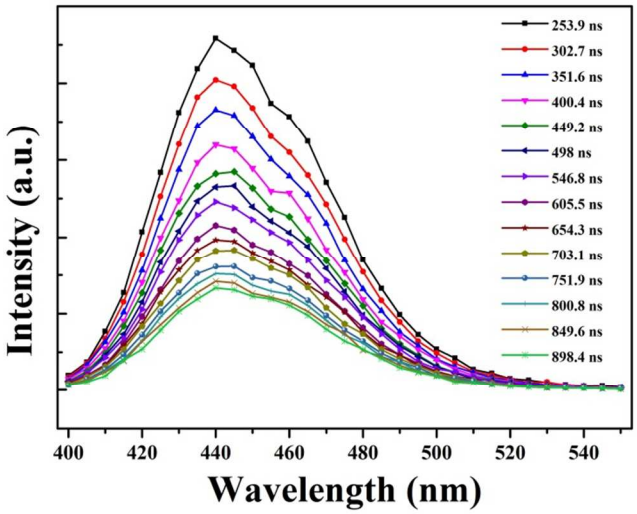

Fig. 9 Time-resolved photoluminescence (TRPL) emission spectra of $BaSc_2Si_3O_{10}$: 0.05Eu^{2+}.

In order to confirm that the broad band emission originates from two luminescent centers, a series of lifetime decay curves were recorded by monitoring the $BaSc_2Si_3O_{10}$: 0.05Eu^{2+} sample at

different wavelengths from 400 to 550 nm at 5 nm intervals. The TRPL spectra shown in Fig. 9 were obtained by slicing them. Obviously, the TRPL spectra are clearly constituted by two emission peaks centered at 440 and 460 nm, which has not been found from the emission spectra shown in Fig. 4. Simultaneously, with the time interval prolonging, it was interesting to observe that the intensity ratio of 440 to 460 nm descended significantly, confirming that there are two light luminescent centers. The occurrence of the two emission peaks further demonstrates Eu^{2+} occupying the two different cationic lattice sites: Ba^{2+} and Sc^{3+} sites. In order to assign the emission from the two luminescent centers, the following equation has been used to build up the relationship between the coordination environment and emission peaks, which is proposed by Van Uitert and successfully used to explain many structure–property relationship studies in Eu^{2+} or Ce^{3+} doped systems.[31]

$$E = Q\left[1 - \left(\frac{V}{4}\right)^{\frac{1}{V}} 10^{-\frac{near}{80}}\right]$$

where E is the position of the rare-earth ion emission peak (cm^{-1}), Q represents the position in energy for the lower d-band edge for the free Eu^{2+} ion (Q = 34 000 cm^{-1} for Eu^{2+}), V is the valence of the "active" cation (V = 2 for Eu^{2+}), n is the number of anions in the immediate shell around the "active" cation, and r is the radius of the host cation occupied by the Eu^{2+} ion (Å). ea is the electron affinity of the atoms that form anions (eV). In $BaSc_2Si_3O_{10}$, the effective ionic radii for Ba^{2+} and Sc^{3+} are 1.42 Å (CN=8) and 0.745 Å (CN=6), respectively. From the equation, one can see that the larger value of $n \times r$, the higher value of E. Therefore, it is obvious that Eu^{2+} occupying the Ba^{2+} position should exhibit a higher-energy (440 nm) emission peak and the Sc^{3+} position reveal emission at 460 nm. Therefore, it can reasonable explained that the emission spectra shift to longer wavelength (red shift) and then to shorter wavelength (blue shift) with the increase of Eu^{2+} concentration in Fig.4.

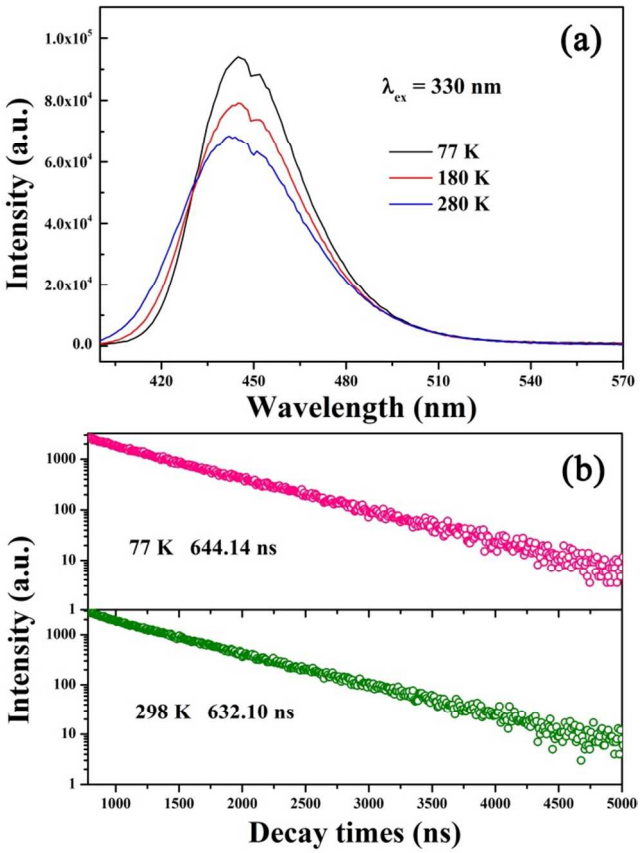

Fig. 10 (a) The temperature dependent emission spectra measured from 77K to 280K, (b) the decay curves of $BaSc_2Si_3O_{10}$: $0.03Eu^{2+}$ under 77 K and 298K.

A series of PL spectra curves of $BaSc_2Si_3O_{10}$: $0.03Eu^{2+}$ measured at different temperature is shown in Fig.10 (a). At low temperature, the emission spectra obviously split into two peaks, which are different from that at room temperature. This result further demonstrates Eu^{2+} occupy Ba^{2+} and Sc^{3+} sites in $BaSc_2Si_3O_{10}$. As increasing the temperature, the emission intensity decrease. The decay curves was measured excited at 375 nm and monitored at 445 nm. The lifetimes at 77 K and 298 K are calculated to be 644.14 ns and 632.10 ns, respectively. The decreased decay times can be attributed to increase interaction between Eu^{2+} when rising temperature.

3.4 Thermally stable luminescence properties

Cite this: DOI: 10.1039/c0xx00000x

www.rsc.org/xxxxxx

ARTICLE TYPE

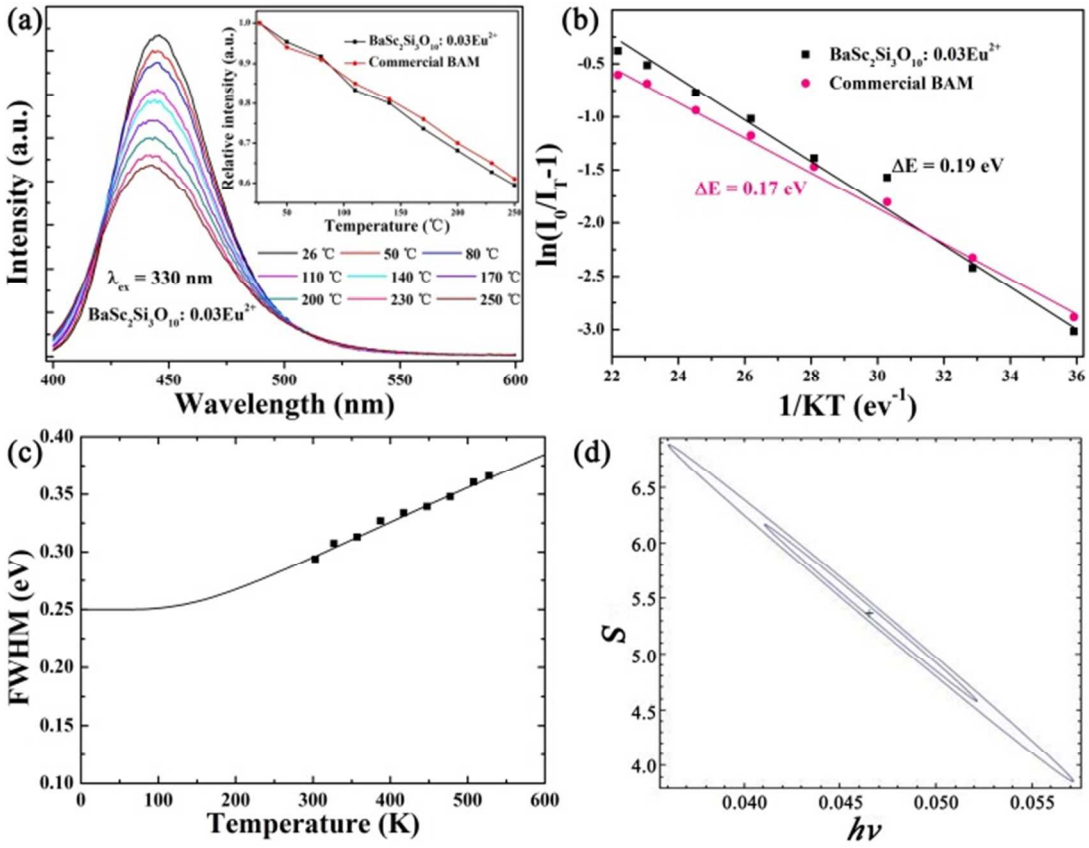

Fig. 11 a) Temperature-dependent PL spectra of $BaSc_2Si_3O_{10}$: $0.03Eu^{2+}$ (The inset shows the thermal stability comparison of $BaSc_2Si_3O_{10}$: $0.03Eu^{2+}$ and the commercial BAM), b) The calculated activation energy for thermal quenching of $BaSc_2Si_3O_{10}$: $0.03Eu^{2+}$ phosphor and the commercial BAM, c) Temperature dependence of FWHM of Eu^{2+} doped $BaSc_2Si_3O_{10}$ and b) the error limit of S and hv.

The thermal stability of phosphors is one of the important parameters for the application in high performance LEDs because it has a considerable influence on the light output and CRI. So the temperature dependent PL properties are investigated and exhibited in Fig. 11(a). Clearly, the emission intensity gradually decrease with increasing temperature, and the intensity decreases to 62 % (at 250 °C) of the initial value. $BaSc_2Si_3O_{10}$: $0.03Eu^{2+}$ shows similar thermal stability to commercial BAM (BAM: 12-1) as can be seen from the insert of Fig. 11(a). Meanwhile, the emission shows a tiny blueshift with increasing temperature, which can be ascribed to the thermally active phonon-assisted tunneling from lower-energy excited states to higher-energy excited state of the configuration coordinate diagram.[32] To better understand the thermal quenching phenomenon, the activation energy (ΔE) for the thermal quenching can be calculated using the Arrhenius equation:[33]

$$I_T = \frac{I_0}{1 + c\exp\left(-\frac{\Delta E}{kT}\right)}$$

where I_0 is the initial PL intensity of the phosphor at room temperature, I_T is the PL intensity at different temperatures, c is a constant, ΔE is the activation energy for thermal quenching, and k is the Boltzmann constant (8.62×10^{-5} eV). According to above equation, the $\ln(I_0/I_T\text{-}1)$ against $1/kT$ is plotted in Fig. 11(b) and the straight slope equals ΔE. The activation energies are calculated to be 0.19 and 0.17 eV for $BaSc_2Si_3O_{10}$: $0.03Eu^{2+}$ and commercial reference blue phosphor, respectively. The results show that $BaSc_2Si_3O_{10}$: $0.03Eu^{2+}$ has a similar thermal stability with commercial BAM.

With increasing temperature, the electron–phonon interaction in both the ground state and excited states of the luminescence center becomes dominant resulting in broadening of the emission spectra and decrease of the emission intensity.[34] The thermal quenching temperature is defined as the temperature at which the PL intensity is 50 % of its initial intensity. In our case, the quenching temperature is obvious above 250 °C. This high quenching temperature indicates the rigid lattice of $BaSc_2Si_3O_{10}$: Eu^{2+} phosphor with weaker electron-phonon interaction. Figure 11(c) and (d) plot the dependence of the full width at half maximum (FWHM) of the emission spectra on various measurement temperatures and the margin of error which were

analyzed using MATLAB software. The FWHM (T) can be described by using the configuration coordinate model and the Boltzmann distribution and expressed by the following equation:[35]

$$\text{FWHM}\ (T) = h\nu[8 \times \ln 2 \times S \times \coth(h\nu/2k_BT)]^{1/2}$$

where hν is the phonon energy, S is the Huang–Rhys parameter, and k_B is the Boltzmann constant. For the $4f^7$ ground state and the $4f^65d$ excited state of Eu^{2+}, $h\nu$ is assumed to be the same. According to the above equation, the best fit is obtained with S = 5.3 ± 0.4 eV and $h\nu$ = 0.04 ±0.0033 eV. The Stokes shift (ΔS) can be estimated from $\Delta S = h\nu \times (2S - 1)$ and ΔS is calculated to be 0.384 eV. The value of Huang–Rhys factor reveals weaker electron–phonon interaction in this phosphor and also provides an evidence for the good thermal photoluminescence property of $BaSc_2Si_3O_{10}$: Eu^{2+}.

3.5 Luminescence quantum efficiency

The quantum efficiency (η) can be obtained by using the following formulas:[36]

$$\varphi = \frac{L_0(\lambda) - L_i(\lambda)}{L_0(\lambda)}$$

$$\eta = \frac{E_i(\lambda) - (1-\varphi)E_0(\lambda)}{E_0(\lambda)\varphi}$$

where $L_0(\lambda)$ is the integrated excitation profile when sample is directly excited by the incident beam and $L_i(\lambda)$ are the integrated excitation profile obtained from the empty integrated sphere (without the sample present). $E_0(\lambda)$ and $E_i(\lambda)$ are the integrated luminescence of powder caused by direct excitation and by indirect illumination from the sphere, respectively. Upon excitation at 330 nm, the external quantum efficiency of this sample is 42.65 %.

4. Conclusion

In conclusion, a series of$BaSc_2Si_3O_{10}$: Eu^{2+}have been prepared by the solid state reaction. $BaSc_2Si_3O_{10}$: Eu^{2+} phosphor shows broad absorption band ranging from 250 to 420 nm, which can match well with the UV-LEDs. The $BaSc_2Si_3O_{10}$: Eu^{2+} exhibits blue broadband emission peaking at 446 nm with a tail on the long wavelength side and CIE coordinates (0.15, 0.05). The concentration quenching mechanism has been carefully investigated to be quadrupole–quadrupole interaction. The Rietveld refinements results and the time-resolved photoluminescence emission spectra are used to study the abnormal emission of Eu^{2+} in $BaSc_2Si_3O_{10}$. The emission intensities of $BaSc_2Si_3O_{10}$: Eu^{2+} dependence on different temperatures show similar thermal property compared with BAM. All results show that the obtained phosphors have potential application in UV excited w-LEDs as blue emitting components.

Acknowledgements:

This work is supported by Specialized Research Fund for the Doctoral Program of Higher Education (no. 20120211130003) and the National Natural Science Funds of China (Grant No. 51372105).

Authors' Address

[a] *Key Laboratory for Magnetism and Magnetic Materials of the Ministry of Education, School of Physical Science and Technology, Lanzhou University, Lanzhou 730000, China.*
[b] *Key Laboratory of Design and Assembly of Functional Nanostructures, Fujian Institute of Research on the Structure of Matter, Chinese Academy of Sciences, Fuzhou, Fujian, 350002 (P. R. China).*

Footnotes

*Corresponding author: wyh@lzu.edu.cn

References

1 S. Ye, F. Xiao, Y. X. Pan, Y. Y. Ma and Q. Y. Zhang, *Mater. Sci. Eng., R*, 2010, **71**, 1.
2 C. C. Lin and R. S. Liu, *J. Phys. Chem. Lett.*, 2011, **2**, 1268.
3 M. M. Shang, C. X. Li and J. Lin, Chem. *Soc. Rev.*, 2014, **43**, 1372.
4 S. S. Hu and W. J. Tang, *J. Mater. Sci.*, 2013, **48**, 5840.
5 P. Zhu, Q. Zhu, H. Zhu, H. Zhao, B. Chen, Y. Zhang, X. Wang and W. Di, *Opt. Mater.*, 2008, **30**, 930.
6 W. B. Im, Y. -I. Kim, H. S. Yoo and D. Y. Jeon, *Inorg. Chem*. 2008, **48**, 557.
7 P. L. Li, Z. J. Wang, Z. P. Yang and Q. L. Guo, *J Mater. Chem. C*, 2014, **2**, 7823.
8 X. H. Gong, J. H. Huang, Y. J. Chen, Y. F. Lin, Z. D. Luo and Y. D. Huang, *Inorg. Chem.*, 2014, **53**, 6607.
9 K. Geng, Z. G. Xia and M. S. Molokeevc, *Dalton Trans.*, 2014, **43**, 14092.
10 J. Chen, Y. G. Liu, M. H. Fang and Z. H. Huang, *Inorg. Chem.*, 2014, **53**, 11396.
1 H. Yu, D. G. Deng, D. T. Zhou, W. Yuan, Q. E. Zhao, Y. J. Hua, S. L. Zhao, L. H. Huang and S. Q. Xu, *J. Mater. Chem. C*, 2013, **1**, 5577.
2 D. G. Deng, H. Yu, Y. Q. Li, Y. J. Hua, G. H. Jia, S. L. Zhao, H. P. Wang, L. H. Huang, Y. Y. Li, C. X. Lia and S. Q. Xu, *J. Mater. Chem. C*, 2013, **1**, 3194.
3 W. J. Yang, L. Y. Luo, T. M. Chen and N. S. Wang, *Chem. Mater.,* 2005**, 17***,* 3883.
4 Z. G. Xia, J. Zhou and Z. Y. Mao, *J. Mater. Chem. C*, 2013, **1**, 5917.
15 S. Ray, Y. C. Fang and T. M. Chen, *RSC Advances*, 2013, **3**, 16387.
16 W. W. Maria, K. Uwe and T. Ekkehart, *Can. Mineral.*, 2010, **48**, 51.
17 Y. F. Liu, X. Zhang, Z. D. Hao, Y. S. Luo, X. J. Wang and J. H. Zhang, *J. Mater. Chem*., 2011, **21**, 16379.
18 G. Zhu, Y. R. Shi, M. Mikami, Y. Shimomurab and Y. H. Wang, *CrystEngComm*, 2014, **16**, 6089
19 M. Wierzbicka-Wieczorek, U. Kolitsch and E. Tillmanns, *Eur. J. Mineral*. 2010, **22**, 245.
20 Y. Wen, Y. H.Wang, B. T. Liu, F. Zhang, Y. R. Shi, *Funct. Mater. Lett*. 2012, **5**, 1250048.
21 R. D. Shannon, *Acta, Cryst.*, 1976, **A32**, 751.
22 M. Y. Peng, Z. W. Pei, G. Y. Hong and Q. Su, *J. Mater. Chem.*, 2003, **13**, 1202.
23 Z. G. Xia, Y. J. Liang, W. Z. Huang, D. Y. Yu, M. F. Zhang and M. H. Tong, *Ceram. Int.*, 2013, **39**, 7097.
24 M. Nikl, K. Nitsch, J. Hybler, J. Chval and P. Reiche, *Phys. Stat. Sol. B* 1996, **196**, K7.
25 G. Blasse and B. C. Grabmaier, Luminescent Materials, *Springer-Verlag*, Berlin, 1994.
26 G. Ju, Y. Hu, L. Chen and X. Wang, *J. Appl. Phys.*, 2012, **111**, 113508.
27 D. L. Dexter, *J. Chem. Phys.*, 1953, **21**, 836.
28 L. Ozawa and P. M. Jaffe, *J. Electrochem. Soc*. 1971, **118**, 1678.
29 W. R. Liu, C. C. Lin, Y. C. Chiu, Y. T. Yeh, S. M. Jang, R. S. Liu, B. M. Cheng, *Opt. Express* 2009, **17**, 18103-18109.
30 N. Ruelle, M. P. Thi and C. Fouassier, *Jpn. J. Appl. Phys.*, 1992, **3**1, 2786.
31 L. G. Van Uitert, *J. Lumin.*, 1984, **29**, 1.

32 J. S. Kim, Y. H. Park, S. M. Kim, J. C. Choi and H. L. Park, *Solid State Commun.*, 2005, **133**, 445.
33 Z. G. Xia, R. S. Liu, K. W. Huang and V. Droid, *J. Mater. Chem.*, 2012, **22**, 15183.
34 V. B. Mikhailikm, H. Kraus, D. Wahl, M. Itoh, M. Koike and I. K. Bailiff, *Phys. Rev. B* 2004, **69**, 20510.
35 D. W. Cooke, B. L. Bennett, K. J. Maclellan, J. M. Roper and M. T. Whittaker, *J. Appl. Phys.*, 2000, **87**, 7793.
36 J. C. de Mello, H. F. Wittmann and R. H. Friend, *Adv. Mater.*, 1997, **9**, 230.